

# Frequency measurements of $5s5p^3P_0 \rightarrow 5s6d^3D_1$ and observation of nonlinearities in King plot with Sr

S. Zhang,\* B. T. Tiwari, S. Ganesh, and Y. Singh†

*School of Physics and Astronomy, University of Birmingham,  
Edgbaston, Birmingham, B15 2TT, United Kingdom*

(Dated: June 22, 2023)

We report the first precision measurement of the absolute frequency of  $5s5p^3P_0 \rightarrow 5s6d^3D_1$  for all four stable Sr isotopes with an accuracy of  $\sim 25$  kHz employing repumping induced spectroscopy. By combining the isotope shifts of this transition with the existing measurement data on the intercombination line, the King plot is established which reveals a deviation from the linearity at the  $5.2\sigma$  level.

## I. INTRODUCTION

Isotope shift (IS) spectroscopy has been playing a crucial role in our understanding of the atomic and nuclear structure [1, 2], mean-square nuclear charge radii [3–5], significant physical parameters within the standard model (SM) of elementary particles [6–9], etc. More recently, the importance of IS has been further emphasized by consecutive successes on the experimental search for new phenomena beyond the SM by employing high-precision atomic isotope shift measurements [10–12]. In general, the ISs between two distinct atomic transitions can be analysed by the so-called linear King plot [13, 14] under the assumption that the IS is composed of the field and mass shifts. However, such a linear relation would be broken when the nonlinear contribution becomes non-negligible [15] within the limit of error, which may arise from higher-order contributions within SM, such as quadratic mass shift, quadratic field shift (QFS), quadrupole nuclear deformation [16, 17] and nuclear polarizabilities [15, 18], or new physics (NP) beyond SM. The new interaction between electrons and neutrons is mediated by a new boson with mass  $m_\phi$ , which would give rise to a Yukawa potential and the resulting isotope shifts. Such shifts could be detected by the deviation from the linearity of King plot with precision IS measurements. While SM nonlinearity (NL) contributions have a limitation to the sensitivity of new physics, this problem could be mitigated by adopting a generalized King plot (GKP) combining IS data of more than two transitions in order to eliminate nonlinearities from SM [19, 20]. Notably, a formalism that constraining fundamental new physics from bounds on King plot nonlinearities without a knowledge of SM effects has recently been developed in Ref. [21].

As the significance of precision IS measurements in searches for new physics beyond SM is apparent, experimental observations of nonlinearities in King plot in alkaline-earth-metal atoms and ions have been intensively emerging more recently, such as  $\text{Ca}^+$  [7, 22, 23],

$\text{Yb}$  [24, 25] and  $\text{Yb}^+$  [26, 27]. In Ref. [23], high-precision frequency-comb Ramsey spectroscopy with an accuracy of 20 Hz improved the sensitivity to NP bosons coupling to both electrons and neutrons in  $\text{Ca}^+$ . Recent work on  $\text{Yb}$  [24] where a  $\sim 2\sigma$  deviation in GKP was obtained suggests that nuclear deformation may account for the NL; in addition, Ref. [25] using the narrow clock transition concludes that the observed NL at the  $\sim 3\sigma$  uncertainty level could be interpreted by at least two various higher-order SM sources, i.e., the QFS and the nuclear deformation. Notably a novel parametrization of the NL pattern was proposed to distinguish different possible physical origins for NL in Ref. [26]; the adjacent work [27], using the highly forbidden octupole transition  $^2\text{S}_{1/2} \rightarrow ^2\text{F}_{7/2}$  of  $\text{Yb}^+$ , evidenced two sources in the obtained nonlinearity increased by 20-fold compared with Ref. [26]. Upon Sr atoms, extensively studied for decades in optical lattice clocks [28–30], superradiant laser [31–33], Bose–Einstein condensation (BEC) [34–36] benefited by its favorable properties, however, till now it has yet been intensively experimentally investigated in search for new physics beyond SM with precision IS measurements [37, 38].

In this letter, we first measure the absolute frequency of  $5s5p^3P_0 \rightarrow 5s6d^3D_1$  with repumping induced spectroscopy (RIS) [37, 39–41] for all Sr isotopes  ${}^A\text{Sr}$  ( $A=84, 86, 87, 88$ ), and perform King plot analysis by referencing the measured IS data to the 689 nm data extracted from Ref. [38]. A 5.2 standard deviation  $\sigma$  nonlinearity is observed in King plot. This work is motivated by the importance of the  $5s5p^3P_0 \rightarrow 5s6d^3D_1$  transition. Firstly, this transition is ideal for repumping of the  ${}^1\text{S}_0 \rightarrow {}^1\text{P}_1$  magneto-optical trap (MOT) like 679 or 707 nm channels but more efficient; secondly, it has long been a barrier on the detection of the scattering light on the  $5s5p^3P_0 \rightarrow 5s4d^3D_1$  transition at  $2.6\ \mu\text{m}$  from long-range interactions [42]. Instead, detecting the fluorescence on the 394 nm transition, which shares the same ground state with the  $2.6\ \mu\text{m}$  transition, enables to dramatically improve the signal-to-noise ratio due to a higher decay rate; finally, having a quite different electronic structure to the two transitions studied in Ref. [38], this transition used in King plot can lead to a higher sensitivity to higher-order effects in nonlinearities [24, 25].

\* s.zhang.3@bham.ac.uk

† Y.Singh.1@bham.ac.uk

## II. EXPERIMENTAL DETAILS

The schematic of the experimental setup and the relevant energy levels for  $^{88}\text{Sr}$  are shown in Fig. 1. Sr atoms with a  $10^{11}\text{s}^{-1}$  flux ejected from an oven were decelerated by a Zeeman slower and captured in a three-dimensional (3D) magneto-optical-trap (MOT) operated on a broad line  $^1\text{S}_0 \rightarrow ^1\text{P}_1$  at 461 nm. The MOT beams, red-detuned by 40 MHz, *i.e.*,  $1.25\Gamma$  ( $\Gamma=32$  MHz), have a total peak intensity of  $0.5\text{I}_s$  and a  $e^{-2}$  radius of 1 cm under the operational condition. The axial magnetic gradient is operating at 55 G/cm. We excited atoms populated in  $^3\text{P}_2$  by 707 nm light back to the cooling cycle through the  $^3\text{P}_2 \rightarrow ^3\text{S}_1 \rightarrow ^3\text{P}_0$  channel. The repump laser was locked to a high precision wavemeter (highfinesse WSU2) with an accuracy of 2 MHz. Driving the  $5s5p^3\text{P}_0-5s6d^3\text{D}_1$  transition at 394 nm enables to enhance the atom number in the steady-state MOT by an order of magnitude in comparison with the repumping-free case, which is the idea of RIS.

Here we carried out RIS to measure the frequency of the  $5s5p^3\text{P}_0 \rightarrow 5s6d^3\text{D}_1$  transition for all stable isotopes. By using the repumping of atoms, this scheme enables us to perform the spectroscopy by observing the repumping enhancement in steady-state MOT atoms. Cooling atoms to  $\sim 1$  mK temperature induces the Doppler broadening much less than the natural linewidth of 14.3 MHz [43]. Pumped by a high-power fibre laser at 532 nm, the probe laser has a frequency tunability of hundreds of GHz. As there is no lab-ready frequency comb to beat with, the frequency of the probe laser was determined by the seed laser frequency at 788 nm which has a connection to a ultrastable clock laser at 698 nm through the transfer cavity locking scheme [44, 45]. The clock laser was stabilized to an ultralow-expansion glass (ULE) cavity with a finesse of  $2.3 \times 10^5$  by means of Pound-Drever-Hall (PDH) technique, resulting in a stability of  $1.1 \times 10^{-14}$  at 1 s. Such a stability was transferred via a transfer cavity to the seed laser, and thus to the probe laser. The frequency of the clock laser can be directly measured by a frequency comb (Menlo Systems Smart comb) which has a repetition frequency  $f_{\text{rr}}=125$  MHz and a carrier envelope offset frequency  $f_{\text{ceo}}=10$  MHz, referenced to an ultrastable laser at 1542 nm with a stability of  $2.2 \times 10^{-15}$  at 1 s average. The beat note between the clock laser and the frequency comb was continuously monitored by a frequency counter referenced to a 10-MHz GPS-disciplined hydrogen maser (iMaser 3000), which has a stability of  $4 \times 10^{-16}$  with an integral of more than 10,000 s. As such, the frequency of the probe laser can be calibrated from the clock laser frequency.

The probe beam was split into two branches. One was for the frequency monitor with a Rb oscillator-referenced wavemeter, the other was delivered to the spectroscopy region in free space, where the counter-propagating configuration was employed to cancel the first-order Doppler shift and corresponding uncertainties. The entire MOT ensemble was illuminated by the probe beam with a 6

mm diameter. The  $^3\text{P}_0, m=0 \rightarrow ^3\text{D}_1, m'=0$  transition was driven by the linearly polarized beam for even isotopes, and  $\pi$  transitions of hyperfine states were excited for the odd isotope. The fluorescence was detected by a camera while scanning the probe laser frequency. The probe laser power was kept at  $0.2\text{I}_s$  with the fluctuation less than 0.1%. After an individual measurement, we optimised experimental parameters to ensure each measurement was performed under the same condition. Each data point of the measurement was an average of five to ten measurements. The RIS was recorded by scanning the probe laser up and down across the resonance. The whole process for data collection lasted four months to cancel out the influence of the lab environment.

## III. RESULTS

### A. Frequency measurements of $5s5p^3\text{P}_0 \rightarrow 5s6d^3\text{D}_1$

The frequency measurement results and corresponding uncertainties for all isotopes were shown in Table I. The absolute frequencies have been measured with an uncertainty of less than 30 kHz. For  $^{87}\text{Sr}$ , we weighted the measurements of three hyperfine manifolds  $F \in \{11/2, 9/2, 7/2\}$  and derived the center of gravity (cog) as well as hyperfine constants A and B. We improved the accuracy of hyperfine constants by two orders of magnitude compared to the previous result in Ref. [39]. Due to the separation of  $5\text{ cm}^{-1}$  between  $^3\text{D}_1$  and  $^3\text{D}_2$ , second-order hyperfine interactions were taken into account in the determination of cog of  $^{87}\text{Sr}$ . Details of theoretical calculation and experimental evaluation for second-order contribution can be seen in Appendix C. In the determination of isotope shifts, the frequencies of  $^{84,86,87}\text{Sr}$  were referenced to  $^{88}\text{Sr}$ . The leading systematic effects and uncertainties were summarized in Table III and IV. The probe power shift, density shift and the misalignment are leading effects, which have a 70~200 kHz shift and a 7~17 kHz uncertainty, while others are less influential. The density-dependent shift is the predominant effect which causes a  $\sim 200$  kHz shift under the operating condition with a density shift coefficient of  $-1.4 \times 10^{-4}$  Hz  $\text{cm}^3$ . The power-induced AC stark shift introduces  $\sim 100$  kHz contribution at  $70\ \mu\text{W}$  with the coefficient  $\kappa = 100.98\ \text{kHz mW}^{-1}\ \text{cm}^2$ . In addition, the probe beam misalignment can shift the resonant frequency, which was verified to be  $\sim 100$  kHz. The detailed analysis of the systematic effects and respective uncertainties can be seen in Appendix D.

### B. King plots analysis

The IS between isotopes  $A$  and  $A'$  can be parameterized, to a good approximation, to an electronic component only dependent on the transition and a nuclear contribution which depends on the isotope. The leading

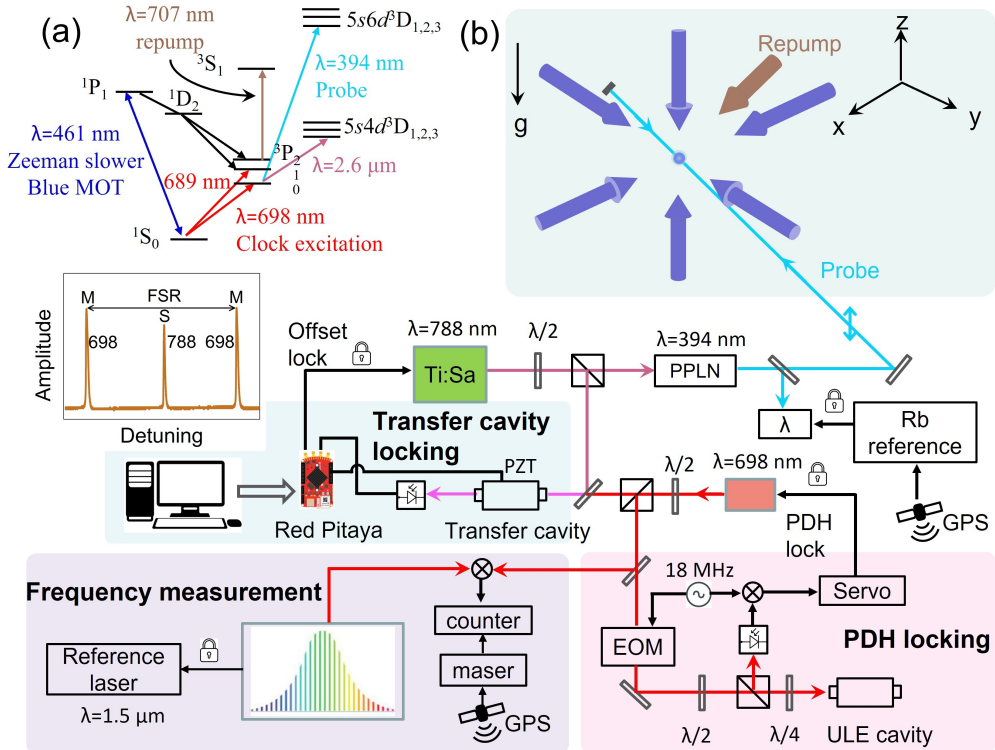


FIG. 1: Schematic diagram of experiment. (a) Relevant energy levels of the Sr atom. We perform precision measurements on the  $5s5p^3P_0 \rightarrow 5s6d^3D_1$  transition at 394 nm. (b) Schematic illustration of experimental setup. The whole setup mainly consists of four parts, i.e., transfer cavity locking, PDH laser stabilization, cold atomic package and frequency comb measurements. The probe laser was generated by frequency doubling the Ti:Sa laser at 788 nm which was locked to an ultrastable clock laser at 698 nm via a transfer cavity with the help of a programmable micro controller (Red Pitaya). The clock laser was stabilized to a vertical cavity with a finesse of  $2.3 \times 10^5$ , and has a 100-Hz linewidth and a  $1.1 \times 10^{-14}$  stability at 1 s. EOM: electro-optic modulator; PPLN: Periodically Poled Lithium Niobate; GPS: Global Positioning System. Our frequency comb was referenced to an ultrastable  $1.5 \mu\text{m}$  laser with a stability of  $2.2 \times 10^{-15}$  of 1 s. All frequency measurements were referenced to a GPS-disciplined hydrogen maser. The atomic ensemble was trapped in a MOT of the  $^1S_0 \rightarrow ^1P_1$  transition with a repump of 707 nm on.

TABLE I: Absolute frequency measurements of  $^3P_0 \rightarrow ^3D_1$  for all Sr isotopes and the ISs relative to  $^{88}\text{Sr}$ . For  $^{87}\text{Sr}$ , the frequency measurement results in the first- and second-order perturbation theory were respectively listed. The hyperfine constants A and B were derived in corresponding cases. Previous results from Refs. [39, 43] were listed for comparison. The numbers in parentheses indicate  $1\sigma$  uncertainty.

Isotopes	Absolute frequency (MHz)	Previous	Isotope shifts (MHz)
$^{88}\text{Sr}$	760524409.251(23)	760524989 <sup>a</sup>	0
$^{84}\text{Sr}$	760524318.199(26)		91.052(35)
$^{86}\text{Sr}$	760524354.651(24)		54.600(33)
	In 1 <sup>st</sup> order	In 2 <sup>nd</sup> order	
$^{87}\text{Sr}, f_{\text{cog}}$	760524336.980(16)	760524357.610(16)	51.641(28) <sup>c</sup>
$^{87}\text{Sr}, F=11/2$	760525416.310(29)	760525438.153(29)	
$^{87}\text{Sr}, F=9/2$	760524087.692(27)	760524111.756(27)	
$^{87}\text{Sr}, F=7/2$	760523029.704(26)	760523044.114(26)	
A	238.984(4)	239.599(4)	239.7(5) <sup>b</sup>
B	15.500(32)	9.382(32)	5(20) <sup>b</sup>

<sup>a</sup> Taken from X. Zhou, *et al.* [43].

<sup>b</sup> Taken from S. Stellmer and F. Schreck [39].

<sup>c</sup> Measured result in 2<sup>nd</sup> order perturbation.

effects in the IS originate from the mass shift and the field shift, the former of which is due to differences in the nuclear recoil energy and the latter stems from differences in electronic potentials near the origin[23]. The IS of the transition  $i$  can be written with these two leading-order terms as

$$\delta\nu_i^{AA'} = \frac{K_i}{\mu^{AA'}} + F_i \delta\langle r_c^2 \rangle^{AA'} \quad (1)$$

Here  $K_i$ ,  $F_i$  denote the electronic mass- and field-shift factors respectively, and  $F_i = E_i f(Z)$  with  $E_i$  being the difference in the electronic density at the nucleus between lower and upper states in the transition  $i$  and  $f(Z)$  being a relativistic correction factor;  $\delta\langle r_c^2 \rangle^{AA'} = \langle r_c^2 \rangle^A - \langle r_c^2 \rangle^{A'}$  is the difference in mean squared charge radii  $r$  between isotopes  $A$  and  $A'$ ;  $1/\mu^{AA'} \equiv 1/m^A - 1/m^{A'}$  is the inverse mass difference. The modified IS  $\overline{\delta\nu_i}^{AA'}$  can be written by multiplying  $\mu^{AA'}$  in Eq. (1) as follows

$$\overline{\delta\nu_i}^{AA'} = K_i + F_i \overline{\delta\langle r_c^2 \rangle}^{AA'} \quad (2)$$

where  $\overline{z}^{AA'} = \mu^{AA'} z^{AA'}$  for  $z \in \{\delta\nu_i, \delta\langle r_c^2 \rangle\}$ . When two distinct transitions  $i$  and  $j$  are considered,  $\delta\langle r_c^2 \rangle^{AA'}$  in Eq. (2) can be eliminated. The linear relation of the modified IS between the two is given by[13]

$$\overline{\delta\nu_i}^{AA'} = K_i - \frac{F_i}{F_j} K_j + \frac{F_i}{F_j} \overline{\delta\nu_j}^{AA'} \quad (3)$$

Thus when plotting the modified IS  $\mu^{AA'} \overline{\delta\nu_i}^{AA'}$  against  $\mu^{AA'} \overline{\delta\nu_j}^{AA'}$  upon Eq. (3), all data points should fit to a straight line, i.e., so-called King plot.

The contribution from higher-order ISs within SM and new physics interactions beyond SM can violate the linear relation [24]. The IS in Eq. (1) is then revised after taking such contributions into account, so that,

$$\delta\nu_i^{AA'} = \frac{K_i}{\mu^{AA'}} + F_i \delta\langle r_c^2 \rangle^{AA'} + G_i^{(2)} (\delta\langle r_c^2 \rangle^2)^{AA'} + G_i^{(4)} (\delta\langle r_c^4 \rangle)^{AA'} + \alpha_{\text{NP}} X_i \gamma^{AA'} \quad (4)$$

where  $G_i^{(2)}$  and  $G_i^{(4)}$  denote the electronic factors associated with the QFS and the next-leading-order Seltzer moment, respectively. The quantities  $\{K, F, G^{(2)}, G^{(4)}, X\}$  are determined by the electronic wave function of the transition  $i$ .  $(\delta\langle r_c^2 \rangle^2)^{AA'} = (\delta\langle r_c^2 \rangle^{AA_0})^2 - (\delta\langle r_c^2 \rangle^{A'A_0})^2$  with  $A_0$  being the reference nucleus. As introduced in Ref. [46],  $(\delta\langle r_c^4 \rangle)^{AA'} = \langle r_c^4 \rangle^{A'} - \langle r_c^4 \rangle^A$ . The quantity  $\alpha_{\text{NP}} = (-1)^{s+1} y_n y_e / (4\pi\hbar c)$  represents the coupling strength of a new boson with mass  $m_\phi$  to the neutron  $y_n$  and electron  $y_e$ , leading to a Yukawa potential given by  $V_\phi(r) = \hbar c \alpha_{\text{NP}} \exp(-r/\lambda_C) / r$ [26, 27] with  $\lambda = \hbar/(m_\phi c)$  being reduced Compton wavelength.  $\gamma^{AA'} = A - A'$  is the change of the neutron number. The coefficient  $X_i$  characterizes the overlap of the wave functions of the lower and upper states of the transition  $i$ , which can be written

TABLE II: Best-fit parameters of King plot in Fig. 2. The values of  $F_{394,689}$  and  $K_{394,689}$  are extracted from the slope and intercept of the linear fitting, respectively. The field shift and mass shift constants  $F$  and  $K$  are derived from the measured isotope shifts and the given values of  $\delta\langle r_c^2 \rangle^{A,88}$ . The units of  $K$  and  $F$  are given by GHz amu and MHz fm $^{-2}$ , respectively.

Parameter	Previous	This work
$F_{394,689}$		-1.336(11)
$K_{394,689}$		1035.7(7.2)
$F_{394}$		1523.5(5.6)
$K_{394}$		-494.9(1.2)
$\delta\langle r_c^2 \rangle^{84,88}$	0.116(3) <sup>a</sup>	
$\delta\langle r_c^2 \rangle^{86,88}$	0.050(2) <sup>a</sup>	

<sup>a</sup> Taken from R. E. Silverans, *et al.* [47].

as[25]

$$X_i = \frac{c}{2\pi} \int_0^\infty dr \delta\rho_i(r) \frac{e^{-mcr/\hbar}}{r} \quad (5)$$

where  $\delta\rho_i(r)$  is the change in the radial electron density function during the transition  $i$ . Thus by taking NL terms into account, Eq. (3) is modified by

$$\overline{\delta\nu_i}^{AA'} = K_{ij} + F_{ij} \overline{\delta\nu_j}^{AA'} + G_{ij}^{(2)} (\overline{\delta\langle r_c^2 \rangle^2})^{AA'} + G_{ij}^{(4)} (\overline{\delta\langle r_c^4 \rangle})^{AA'} + \alpha_{\text{NP}} X_{ij} \gamma^{AA'} \quad (6)$$

where the electronic factors are defined as  $F_{ij} \equiv F_i/F_j$ ,  $H_{ij} \equiv H_i - F_{ij} H_j$  for  $H \in \{K, G^{(2)}, G^{(4)}, X\}$ .

The King plot was established with the isotope shifts of the transition  $\gamma$ :  $^3\text{P}_0$ - $^3\text{D}_1$  in this work in combination with the data of the intercombination transition  $\alpha$ :  $^1\text{S}_0$ - $^3\text{P}_1$  taken from Ref. [38], as shown in Fig. 2. The blue straight line is a best fit to three experimental data points following Eq. (3). The value of  $\chi^2$ , namely, the residual sum of squares, was minimized to be 79.06 for one degree of freedom. The fitted line yields a slope of  $F_{394}/F_{689} = -1.336 \pm 0.011$  and an intercept of  $K_{394} - F_{394}/F_{689} \cdot K_{689} = 1035.71 \pm 7.20$  GHz amu. However, the zoomed-in insets, where the error bars indicate  $1\sigma$  uncertainty, reveal the NL at the order of  $5.2\sigma$  significance. The best-fit parameters of King plot are summarized in Table II.

By substituting  $1/\mu^{AA'}$  in Eq. (6) with  $\overline{\delta\nu_j}^{AA'}$ , it can be written as the frequency-normalized King plot formulated by

$$\overline{\overline{\delta\nu_i}}^{AA'} = \frac{K_{ij}}{\overline{\mu}^{AA'}} + F_{ij} + G_{ij}^{(2)} (\overline{\overline{\delta\langle r_c^2 \rangle^2}})^{AA'} + G_{ij}^{(4)} (\overline{\overline{\delta\langle r_c^4 \rangle}})^{AA'} + \alpha_{\text{NP}} X_{ij} \overline{\gamma}^{AA'} \quad (7)$$

where all parameters are defined the same as above except  $\overline{\overline{z}}^{AA'} = z^{AA'} / \overline{\delta\nu_j}^{AA'}$  for  $z \in \{\delta\nu_i, \mu, \delta\langle r_c^2 \rangle^2, \delta\langle r_c^4 \rangle, \gamma\}$ . The first two terms are the linear relation between  $\overline{\overline{\delta\nu_i}}^{AA'}$

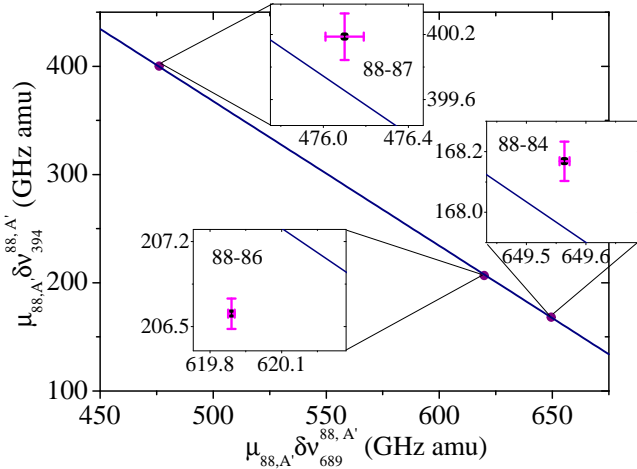


FIG. 2: 2D King plot of  $\gamma$ : 394 nm  $^3P_0 \rightarrow ^3D_1$  versus  $\alpha$ : 689 nm  $^1S_0 \rightarrow ^3P_1$ . The data for 689 nm is from Ref. [38]. The solid line is a fit to the data points with Eq. (3). The extracted fit parameters are given in the text. The insets show the details at each isotope pair with error bars meaning  $1\sigma$  uncertainty. A deviation from the best-fit line by  $5.2\sigma$  is observed.

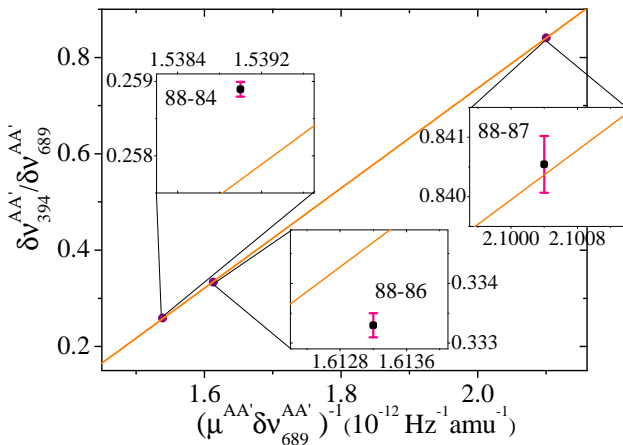


FIG. 3: Frequency-normalized King plot for the 394 nm and 689 nm transitions. The orange line is a fit to all three data points with Eq. (7). The insets for each isotope pair are shown and the error bars represent  $1\sigma$  uncertainty. The derived intercept is equal to the slope of Fig. 2.

and  $1/\bar{\mu}^{AA'}$  and the rest of the terms account for the nonlinearity in King plot. Fig. 3 shows the frequency-normalized King plot by normalizing  $\delta\nu_{394}$  and  $1/\mu$  to  $\delta\nu_{689}$ . The error bar along the horizontal axis was not denoted since the slope is extremely small, resulting in a negligible mass uncertainty. The fit was obtained with  $\chi=117.47$  for one degree of freedom. The deviation between the fitted line and three data points were confirmed from the enlarged insets, which reveals potential sources for the NL in King plot.

#### IV. CONCLUSIONS

In conclusion, we presented the first precision absolute frequency measurement of the  $5s5p^3P_0 \rightarrow 5s6d^3D_1$  transition for four isotopes  $^{84,86,87,88}\text{Sr}$  with an accuracy of  $\sim 25$  kHz by the repumping induced spectroscopy. In determining the frequency of  $^{87}\text{Sr}$ , the second-order hyperfine interaction was theoretically calculated, which was compared with the experimental extraction from 2D King plot. We measured isotope shifts for all isotopes and carried out the King plot analysis by combining this data with that of the intercombination transition, which shows that a  $5.2\sigma$  nonlinearity was observed.

#### ACKNOWLEDGMENTS

We thank Prof. Victor V. Flambaum and Dr Vladimir A. Dzuba for insightful discussions. We thank Sarah for her contribution on the stabilization of the clock laser. This work was supported by European Union's Horizon 2020 Research and Innovation Programme under the Marie Skłodowska-Curie grant agreement No. 860579 (MoSaiQC Project) and No. 820404 (iqClock project).

#### Appendix A: RIS MEASUREMENTS OF $^{84,86,87,88}\text{SR}$

The absolute frequency of  $^3P_0 \rightarrow ^3D_1$  for  $^{84,86,87,88}\text{Sr}$  was measured with RIS. The procedure of the measurements is briefly summarized as follows. Sr atoms were continuously loaded in a  $^1S_0 \rightarrow ^1P_1$  MOT following Zeeman slower with the 707 nm repumper switched on. As such, the atom number in the MOT stays stable under the working condition unless another repumper at 394 nm brings the  $^3P_0$  atom back to the cooling cycle via the  $^3P_0 \rightarrow ^3D_1 \rightarrow ^3P_1 \rightarrow ^1S_0$  channel. The 394 nm probe laser then illuminated the MOT atoms at a low power, normally at  $70 \mu\text{W}$ , leading to the increased atom number in the MOT. The atomic fluorescence was collected and detected by a camera. The counterpropagating configuration was employed for the probe laser to cancel the first-order Doppler shift. For measuring the transition frequency of various isotopes, the MOT was tuned to work at the respective frequency of  $^1S_0 \rightarrow ^1P_1$ . At resonance, the MOT atom number was enhanced by a factor of four with the 394 nm repumper at  $70 \mu\text{W}$  on with respect to off. Here the repumping efficiency was compared between 394 nm and  $2.6 \mu\text{m}$  transitions, which reveals the former is more efficient. We investigated the leading systematic shifts in the frequency measurement, see Appendix D. The accuracy of frequency measurements depends on the accuracy of the measurement tool, e.g., wavemeter and frequency comb. The wavemeter normally has a MHz-level accuracy, while the frequency comb is cable of mHz accuracy. Unfortunately, for 394 nm, we lack such a frequency comb to directly beat with the 394 nm

laser beam. To improve the accuracy in the determination of the probe frequency, we circumvented the aforementioned barrier by connecting the probe frequency to our ultrastable clock laser by the transfer cavity locking scheme, see Appendix B.

Typical line shapes for all isotopes are shown in Fig. 4. The data points were fitted by a Lorentzian function. The RIS linewidth was evaluated to be 30-50 MHz which is broadened primarily by the magnetic field gradient 55 G/cm of the MOT. The linewidth for  $^{84}\text{Sr}$  was larger than other isotopes, which can be attributed to the higher magnetic gradient used to improve the  $^{84}\text{Sr}$  atom number.

## Appendix B: TRANSFER CAVITY LOCKING

There exists two reasons that we apply the transfer cavity locking scheme to the probe laser. First, there doesn't exist a frequency comb in our lab to measure the frequency of 394 nm laser; second, locking the probe laser to the wavemeter with an accuracy of 2 MHz limits the precision of measurements. Therefore, to tackle the aforementioned issue, we linked the probe laser to our ultrastable clock laser at 698 nm which can be measured in frequency with our frequency comb (MenloSystems SmartComb). Through this scheme, the accuracy of the probe laser frequency would be determined by that of the clock laser. Specifically, we will lock the 788 nm laser before the frequency doubler to the clock laser, which was stabilized to a high-finesse cavity, through a transfer cavity, and derive the probe laser frequency by doubling the frequency of 788 nm which can be known from the relation to the clock laser frequency. While this is an indirect frequency evaluation for the probe laser, it can dramatically improve the accuracy of the probe laser frequency by orders of magnitude with respect to measurements by wavemeter. The frequencies obtained by this method were cross checked with the wavemeter measurements.

In the transfer cavity locking scheme, the stability of the master laser will be transferred to the slave laser by locking the slave laser to the cavity referenced to the master laser. The experimental implementation is described as follow. The superimposed beams of 788 nm (slave) and 698 nm (master) are coupled into the transfer cavity (FPI 100-0750-3V0, Toptica), the transmission signal are detected by a photodiode (PD) and input to a Python-programmed microcontroller (Red Pitaya STEMlab 125-10); While scanning the cavity slightly over one free spectrum range (FSR) of 1 GHz, the transmission peaks for two beams will be detected simultaneously; From the start of trigger, the peak position will be set in an order of master-slave-mater. By executing the algorithm for peak detection, an error signal will be generated and fed back to the cavity controller as well as the slave laser controller to lock them to the master laser.

The slave frequency  $f_s$  can be expressed by the master

frequency  $f_m$  [44],

$$f_s = \frac{N_s}{N_m} (\Delta_{\text{FSR}} r + f_m) \quad (\text{B1})$$

where  $N_m$ ,  $N_s$  are the master and slave mode numbers, respectively;  $r = \frac{t_m - t_s}{t_{m'} - t_m}$  is the ratio of the timing interval between master and slave peaks to FSR. Mode numbers can be estimated from the wavemeter measurement; where  $f_m$  is measured by the frequency comb given by

$$f_m = N f_{\text{rr}} + f_{\text{ceo}} - f_{\text{beat}} \quad (\text{B2})$$

where  $f_{\text{ceo}} = 10$  MHz,  $f_{\text{rr}} = 125$  MHz. By substituting  $f_m$  in Eq. (B1) with Eq. (B2), the probe laser frequency can, therefore, be derived.

The frequency resolution  $\Delta f$  of the locking system is limited by the clock speed  $\Delta t$  of the microcontroller and the scanning rate  $f_{sr}$ , given by[45]

$$\Delta f = 2\Delta_{\text{FSR}} f_{sr} \Delta t \quad (\text{B3})$$

where  $\Delta t = 10$  ns,  $f_{sr} = 1$  kHz. Hence, this allows the locking system to posses the frequency resolution of 10 kHz, which is good enough for our isotope shift measurements.

The clock laser is PDH-stabilized to a vertical cavity (finesse= $2.3 \times 10^5$ , cavity length=78 cm). By beating with another clock laser system (MenloSystems ORS Ultrastable lasers), we obtained the linewidth of the clock laser of  $\sim 100$  Hz. We measured its stability by the beat-note between the laser and the frequency comb, the result is shown in Fig. 5. The 1 s fractional stability is  $1.1 \times 10^{-14}$ , corresponding to 4.7 Hz. The drift of the Allan deviation is attributed to the temperature drift of the cavity length.

To evaluate the locking performance of the slave laser, we measured the Allan deviation over a range of 1~1000 s timescales and compared it with the free running case. Fig. 5 illustrates that the stability of the stabilized slave laser is improved within the whole range with respect to the free-running laser, in particular the 700 s stability improved by a factor of 6000, which confirms that the long term stability of the clock laser is transferred to the 788 nm laser. The best achievable stability is limited by the response speed of PZT of the cavity, which can be understood, from Ref [48], that the laser noise is able to be probed only at frequencies less than half of the scanning rate and the feedback signal is effective only at the frequency below 1/4 of the scanning rate. We have a maximum scanning rate of 1 kHz which limits the locking loop bandwidth to 250 Hz.

## Appendix C: SECOND-ORDER CONTRIBUTION

### 1. Theoretical calculation

In the evaluation of hyperfine splittings, it is sufficient, in most situation, that considering only the first-order

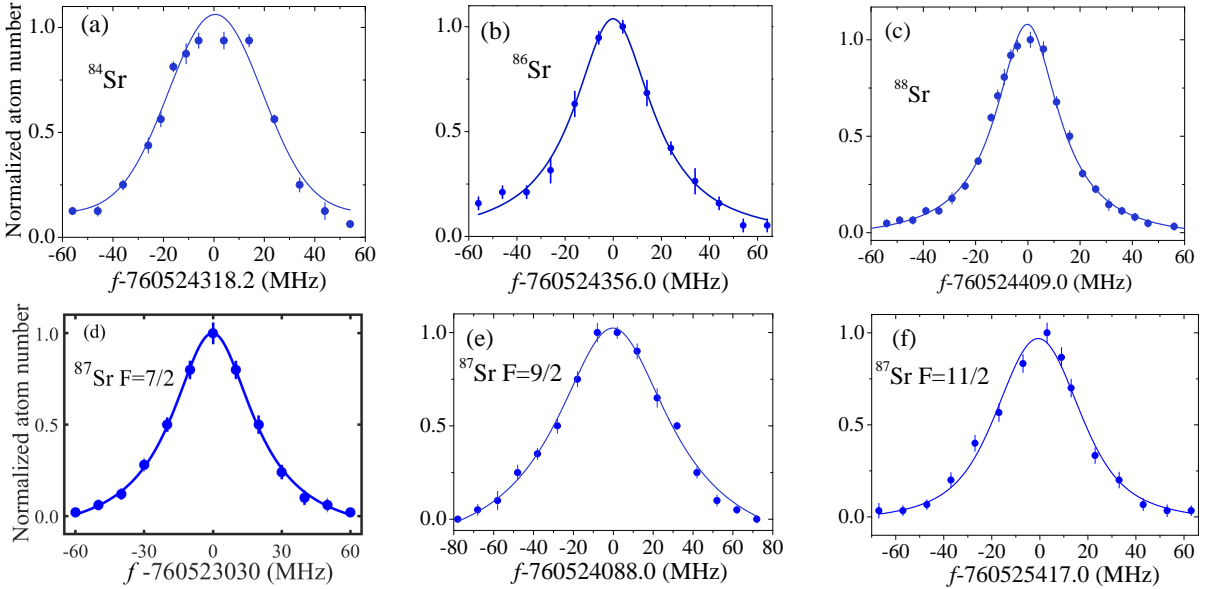


FIG. 4: Typical examples of RIS of  ${}^3P_0 \rightarrow {}^3D_1$  for all Sr isotopes. All measurements were performed at  $70 \mu\text{W}$ . The measurement for  ${}^{84}\text{Sr}$  was carried out at higher oven temperature and higher magnetic field in order to increase the atom number in the ensemble, which results in broader spectroscopic linewidth. Each data point was the average of 5-10 measurements. The atom number was normalized. The solid line is a Lorentzian fit to data. The error indicates  $1\sigma$  uncertainty.

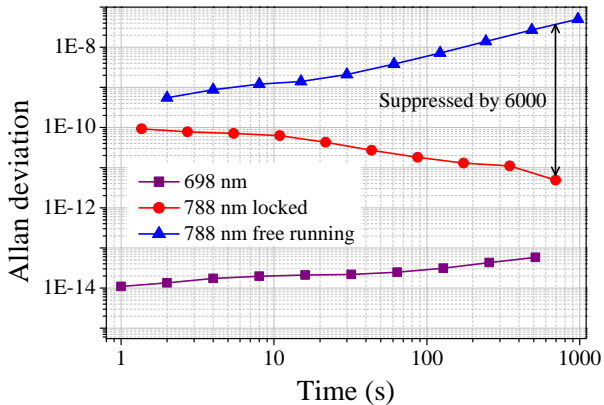


FIG. 5: Fractional frequency stability for the master and slave lasers. The Allan deviation of the locked slave laser is decreased compared with that when free running, showing that a decrease by a factor of 6000 in Allan deviation at 700 s. The short-term stability of the slave laser is limited by the bandwidth  $\sim 250 \text{ Hz}$  of the locking loop.

perturbation theory. However, when the level separation is considerably small, e.g.,  $< 10 \text{ cm}^{-1}$ , the second-order

contribution has to be included, especially in the King plot analysis [49]. From NIST spectra database [50], it's known that the separation between  $5s6d {}^3D_1$  and  ${}^3D_2$  is  $5 \text{ cm}^{-1}$ , which means the second-order effect cannot be neglected here. In this section, we will introduce the calculation of second-order hyperfine splittings for all three hyperfine folds and the correction of the center of gravity as well as hyperfine constants. In addition, we will evaluate the second-order shift from the experimental point of view by 2D King plot.

The second-order hyperfine splitting of the state  $|\gamma JIF\rangle$  is given by

$$\Delta E_F^{(2)} = \sum_{\gamma' J' \neq \gamma J} \frac{|\langle \gamma JIF | H_{\text{hfs}} | \gamma' J' IF \rangle|^2}{E_{\gamma J} - E_{\gamma' J'}} \quad (\text{C1})$$

where  $|\gamma JIF\rangle$  and  $|\gamma' J' IF\rangle$  represent  ${}^3D_1, F\rangle$  and  ${}^3D_2, F\rangle$ , respectively; The Hamiltonian  $H_{\text{hfs}} = H_\mu + H_Q$  consisting of magnetic dipole interactions  $H_\mu$  and electric quadrupole interactions  $H_Q$ ,  $E({}^3D_1) - E({}^3D_2) = 5 \text{ cm}^{-1}$ .

Explicit expressions of hyperfine interaction matrix elements are given by [51, 52]

$$\begin{aligned} \langle l_1 l_2 S L J I F | H_\mu | l_1 l_2 S' L' J' I F \rangle = & (-1)^{J'+I+F} \sqrt{I(I+1)(2I+1)} \begin{Bmatrix} J & I & F \\ I & J' & 1 \end{Bmatrix} \\ & \times \left( l_1 l_2 S L J \left\| \sum_{i=1}^2 a_{l_i} [\mathbf{l}^{(1)} - \sqrt{10} (\mathbf{s}^{(1)} \times \mathbf{c}^{(2)})^{(1)}] + a_{s_i} \delta_{l_i,0} \mathbf{s}^{(1)} \right\| l_1 l_2 S' L' J' \right) \end{aligned} \quad (\text{C2})$$

where

$$\begin{aligned} \left( l_1 l_2 S L J \left\| \sum_{i=1}^2 a_{l_i} \mathbf{l}^{(1)} \right\| l_1 l_2 S' L' J' \right) = & (-1)^{S+L'+J+l_1+l_2} \sqrt{(2J+1)(2J'+1)(2L+1)(2L'+1)} \begin{Bmatrix} L & J & S \\ J' & L' & 1 \end{Bmatrix} \\ & \times \left[ \langle a_{l_1} \rangle (-1)^{L'} \sqrt{l_1(l_1+1)(2l_1+1)} \begin{Bmatrix} l_1 & L & l_2 \\ L' & l_1 & 1 \end{Bmatrix} + \langle a_{l_2} \rangle (-1)^L \sqrt{l_2(l_2+1)(2l_2+1)} \begin{Bmatrix} l_2 & L & l_1 \\ L' & l_2 & 1 \end{Bmatrix} \right] \delta_{S,S'} \end{aligned} \quad (\text{C3})$$

$$\begin{aligned} \left( l_1 l_2 S L J \left\| \sum_{i=1}^2 a_{l_i} (\mathbf{s}^{(1)} \times \mathbf{c}^{(2)})^{(1)} \right\| l_1 l_2 S' L' J' \right) \\ = & (-1)^{l_1+l_2} \frac{3}{\sqrt{2}} \sqrt{(2J+1)(2J'+1)(2L+1)(2L'+1)(2S+1)(2S'+1)} \begin{Bmatrix} \frac{1}{2} & S & \frac{1}{2} \\ S' & \frac{1}{2} & 1 \end{Bmatrix} \begin{Bmatrix} S & S' & 1 \\ L & L' & 2 \\ J & J' & 1 \end{Bmatrix} \\ & \times \left[ \langle a_{l_1} \rangle (-1)^{S'+L'} (l_1 \|\mathbf{c}^{(2)}\| l_1) \begin{Bmatrix} l_1 & L & l_2 \\ L' & l_1 & 2 \end{Bmatrix} + \langle a_{l_2} \rangle (-1)^{S+L} (l_2 \|\mathbf{c}^{(2)}\| l_2) \begin{Bmatrix} l_2 & L & l_1 \\ L' & l_2 & 2 \end{Bmatrix} \right] \end{aligned} \quad (\text{C4})$$

$$\begin{aligned} \left( l_1 l_2 S L J \left\| \sum_{i=1}^2 a_{s_i} \delta_{l_i,0} \mathbf{s}^{(1)} \right\| l_1 l_2 S' L' J' \right) = & (-1)^{S+L+J'+1} \sqrt{\frac{3}{2}} \sqrt{(2J+1)(2J'+1)(2S+1)(2S'+1)} \\ & \times \begin{Bmatrix} S & J & L \\ J' & S' & 1 \end{Bmatrix} \begin{Bmatrix} \frac{1}{2} & S & \frac{1}{2} \\ S' & \frac{1}{2} & 1 \end{Bmatrix} [(-1)^{S'} \langle a_{s_1} \rangle \delta_{l_1,0} + (-1)^S \langle a_{s_2} \rangle \delta_{l_2,0}] \delta_{L,L'} \end{aligned} \quad (\text{C5})$$

and

$$\begin{aligned} \langle l_1 l_2 S L J I F | H_Q | l_1 l_2 S' L' J' I F \rangle \\ = & (-1)^{J'+I+F+1} \sqrt{\frac{(2I+3)(2I+1)(I+1)}{4I(2I-1)}} \begin{Bmatrix} J & I & F \\ I & J' & 2 \end{Bmatrix} \left( l_1 l_2 S L J \left\| e^2 Q \sum_{i=1}^2 r_i^{-3} \mathbf{c}^{(2)} \right\| l_1 l_2 S' L' J' \right) \end{aligned} \quad (\text{C6})$$

where

$$\begin{aligned} \left( l_1 l_2 S L J \left\| e^2 Q \sum_{i=1}^2 r_i^{-3} \mathbf{c}^{(2)} \right\| l_1 l_2 S' L' J' \right) \\ = & (-1)^{S+L'+J+l_1+l_2} \sqrt{(2J+1)(2J'+1)(2L+1)(2L'+1)} \begin{Bmatrix} L & J & S \\ J' & L' & 2 \end{Bmatrix} \\ & \times \left[ \langle b_{l_1} \rangle (-1)^{L'} (l_1 \|\mathbf{c}^{(2)}\| l_1) \begin{Bmatrix} l_1 & L & l_2 \\ L' & l_1 & 2 \end{Bmatrix} + \langle b_{l_2} \rangle (-1)^L (l_2 \|\mathbf{c}^{(2)}\| l_2) \begin{Bmatrix} l_2 & L & l_1 \\ L' & l_2 & 2 \end{Bmatrix} \right] \delta_{S,S'} \end{aligned} \quad (\text{C7})$$

To calculate matrix elements, we reduced to the calculation of single-particle matrix elements  $\langle a_l \rangle$  and  $\langle b_l \rangle$ . For the  $5s6d$  configuration, the expression of  $\langle a_{6d} \rangle$  and  $\langle b_{6d} \rangle$ , according to Sobel'man, can be well approximated by in-

roducing  $a_{5s}$ , given by [51, 53]

$$\langle a_{6d} \rangle = \frac{3}{8} \frac{a_{5s}}{l(l+1)(l+\frac{1}{2})} \left( \frac{\varepsilon_{6d}}{\varepsilon_{5s}} \right)^{3/2} \quad (\text{C8})$$

$$\langle b_{6d} \rangle = \frac{3}{4} \frac{Q}{a_0^2} \frac{a_{5s}}{\alpha^2 g_I \frac{m}{m_p}} \frac{1}{l(l+1)(l+\frac{1}{2})} \left( \frac{\varepsilon_{6d}}{\varepsilon_{5s}} \right)^{3/2} \quad (\text{C9})$$

where  $g_I=0.2428$ ,  $a_0 = 5.2917 \times 10^{-11}$  m,  $Q = 0.335 \times 10^{-28}$  m<sup>2</sup>,  $a_{5s} = -1001(2)$  MHz;  $\varepsilon_{5s}$  and  $\varepsilon_{6d}$  being binding energies of the 5s and 6d orbits [54] are 5.69 eV, 0.77 eV, respectively. By taking these values into Eqs. (C8) and (C9),  $\langle a_{6d} \rangle$  and  $\langle b_{6d} \rangle$  were calculated to be -1.25 MHz and -1.26 Hz, respectively. The values for  $\{l_1, l_2, S, S', L, L', J, J', I\}$  are assigned to be {0, 2, 1, 1, 2, 2, 1, 2, 9/2}. The element  $(l\|\mathcal{C}^{(2)}\|l) = -\sqrt{\frac{l(l+1)(2l+1)}{(2l+3)(2l-1)}}$  was calculated for  $l_1$  and  $l_2$ , i. e.,  $(l_1\|\mathcal{C}^{(2)}\|l_1) = 0$ ,  $(l_2\|\mathcal{C}^{(2)}\|l_2) = -1.2$ . As a result,  $(l_1 l_2 S L J \left\| \sum_{i=1}^2 a_{l_i} (\mathbf{s}^{(1)} \times \mathcal{C}^{(2)})^{(1)} \right\| l_1 l_2 S' L' J') = 0$ ,  $(l_1 l_2 S L J \left\| \sum_{i=1}^2 a_{s_i} \delta_{l_i, 0} \mathbf{s}^{(1)} \right\| l_1 l_2 S' L' J') = -1061$  MHz and  $(l_1 l_2 S L J \left\| \sum_{i=1}^2 a_{l_i} \mathbf{l}^{(1)} \right\| l_1 l_2 S' L' J') = -2.65$  MHz. For the electric quadrupole interaction, the matrix element  $(l_1 l_2 S L J \left\| e^2 Q \sum_{i=1}^2 r_i^{-3} \mathcal{C}^{(2)} \right\| l_1 l_2 S' L' J')$  is calculated to be negligible, indicating the magnetic dipole-electric quadrupole interaction is negligible with respect to the magnetic dipole interaction. Accordingly, the second-order hyperfine splittings were derived to be  $\Delta E_F^{(2)} = 14.4, 24.1, 21.9$  MHz for  $F=11/2, 9/2, 7/2$ , respectively. The center of gravity of  ${}^3D_1$  was corrected by 20 MHz following the relation of  $\Delta E_{\text{cog}} = \frac{2}{5} \Delta E_{11/2} + \frac{1}{3} \Delta E_{9/2} + \frac{4}{15} \Delta E_{7/2}$ .

## 2. Experimental evaluation

The 2D King plot for  $\gamma : {}^3P_0 \rightarrow {}^3D_1$  and  $\alpha : {}^1S_0 \rightarrow {}^3P_1$  transitions before correcting the second-order contribution to the IS of  ${}^{87}\text{Sr}$  is shown in Fig. 6. The King plot line is determined by a linear fitting to even isotope shifts only. The odd modified IS data point is plotted which sits far away from the straight line as a result of the second-order hyperfine interaction on the  ${}^3D_1$  state. The reference transition  $\alpha$  is free from second-order hyperfine interactions within limits of error. To extract second-order hyperfine correction of the isotope shift on the  $\gamma$  transition for  ${}^{87}\text{Sr}$ , we calculated the difference between the experimentally measured IS and the predicted value from King plot line determined only by even isotope shifts. Based on the fitted line, the modified IS of  ${}^{87}\text{Sr}$  of the  $\gamma$  transition is predicted to be 392.8621 GHz amu, which is much less than the experimental measurement result of 553.2741 GHz amu. The difference of modified IS 160.412 GHz amu reveals the second-order contribution of 20.95 MHz, which is consistent with the theoretically calculated result of 20 MHz. The second-order contribution here refers to the shift of the centre of gravity of  ${}^3D_1$  due to second-order hyperfine interaction.

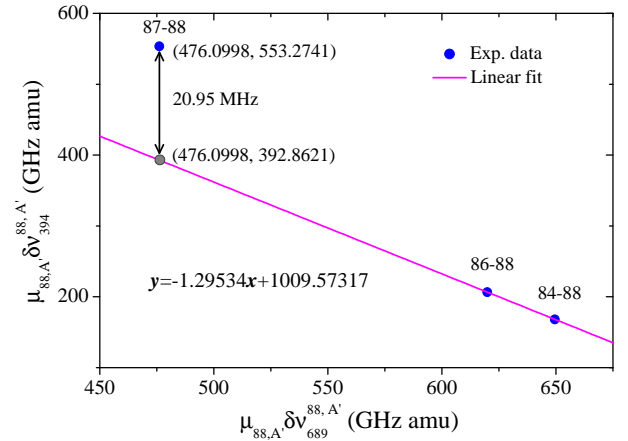


FIG. 6: 2D King plot of  $\gamma$  and  $\alpha$  transitions before correcting the second-order contribution to the IS of  ${}^{87}\text{Sr}$ . The blue dots represent the experimental data and the magenta line is a linear fit to the even isotope shifts only. The gray dot for  ${}^{87}\text{Sr}$  is predicted from the fitted line. The difference of modified IS between the experimental measurement and the prediction is 160.412 GHz amu, corresponding to 20.95 MHz frequency shift, which is primarily due to the second-order contribution.

## Appendix D: SYSTEMATIC EFFECTS AND UNCERTAINTIES

### 1. Density shift

The density dependent frequency shift [55, 56] is one of leading systematic effects in our experiment. We experimentally determined this effect by performing spectroscopic measurements at various atomic densities ranging from  $10^9$  to  $4 \times 10^{11}$  cm<sup>-3</sup>. The density was varied by changing the oven temperature or the magnetic field gradient. The maximum density can reach  $4 \times 10^{11}$  cm<sup>-3</sup> by optimizing the magnetic field at  $\sim 65$  G/cm and the oven temperature at 1063 K. For measurements at each density, the operating probe power was set at 70  $\mu\text{W}$  to minimize the probe power-induced AC stark shift. The ensemble was operating at the density of  $2 \times 10^9$  cm<sup>-3</sup>. To extract the density shift, we applied a linear fit to the experimental data and extrapolated to zero density. Fig. 7 illustrates a typical example of the density-dependent frequency shift as a function of the density from  $4 \times 10^9$  to  $4 \times 10^{10}$  cm<sup>-3</sup> for  ${}^{88}\text{Sr}$ , which reveals the density shift coefficient of  $-1.4 \times 10^{-4}$  Hz cm<sup>3</sup>. The inset shows spectra at  $1.2 \times$  and  $4 \times 10^{10}$  cm<sup>-3</sup> density and fits with Lorentzian function, which depicts the resonance frequency is red detuned by 3.8 MHz accompanied by linewidth broadening when the density was increased from  $1.2 \times 10^{10}$  to  $4 \times 10^{10}$  cm<sup>-3</sup>. Note that the frequency measurement for  ${}^{84}\text{Sr}$  was performed only under the density of  $10^9 \sim 10^{10}$  cm<sup>-3</sup> due to its low abundance.

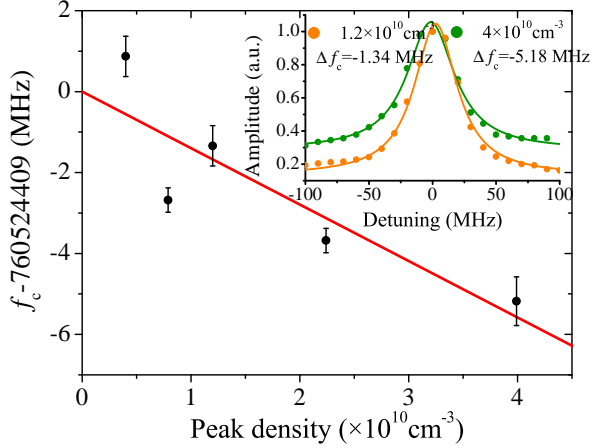


FIG. 7: Dependence of line centre of  ${}^3P_0 \rightarrow {}^3D_1$  on the peak density from  $4 \times 10^9$  to  $4 \times 10^{10} \text{ cm}^{-3}$  for  ${}^{88}\text{Sr}$ . The filled circles and error bars are data and  $1\sigma$  uncertainty, respectively. The red line is a fit. The density shift coefficient is  $-1.4 \times 10^{-4} \text{ Hz cm}^3$ . The inset shows the spectra with a Lorentzian fit for densities of  $1.2 \times$  and  $4 \times 10^{10} \text{ cm}^{-3}$ .

## 2. Probe power shift

Another leading systematic contributor is the probe power-induced AC stark shift [9] arising from differential polarizabilities of  ${}^3P_0$  and  ${}^3D_1$  states. To evaluate this shift  $\kappa I$  (where  $\kappa$  is the shift coefficient,  $I$  is the probe intensity), we drove the  ${}^3P_0$ - ${}^3D_1$  transition with the probe laser for various intensities in a range of  $0.2 \sim 3I_S$  (where  $I_S = 4.76 \text{ mW/cm}^2$  being the saturation intensity of this transition), and extrapolated to zero intensity by the linear fit for all isotopes. Fig. 8 shows the power-induced frequency shift. At each point, we scanned the probe frequency up and down crossing the resonance to average hysteresis effects. An example of the probe power shift for  ${}^{88}\text{Sr}$  is illustrated in Fig. 8(a). The red line is a fit to the data points, revealing the power shift efficient  $\kappa = 100.98 \text{ kHz mW}^{-1} \text{ cm}^2$ . At the operating power of  $70 \mu\text{W}$  the shift is  $\sim 100 \text{ kHz}$  with respect to zero point. The inset shows the spectra under two different powers, which indicates the frequency is shifted by  $3.1 \text{ MHz}$  under  $600 \mu\text{W}$  relative to  $40 \mu\text{W}$ . The same measurement procedure was repeated 10 times for each isotope. After each measurement, the setup including laser polarization and beam alignment was optimized to ensure all data were recorded under the same condition. Fig. 8(b) shows the mean value of the frequency shift for  ${}^{88}\text{Sr}$  as  $94 \text{ kHz}$  and the  $1\sigma$  uncertainty as  $13 \text{ kHz}$ . The final results are listed in Table III and IV.

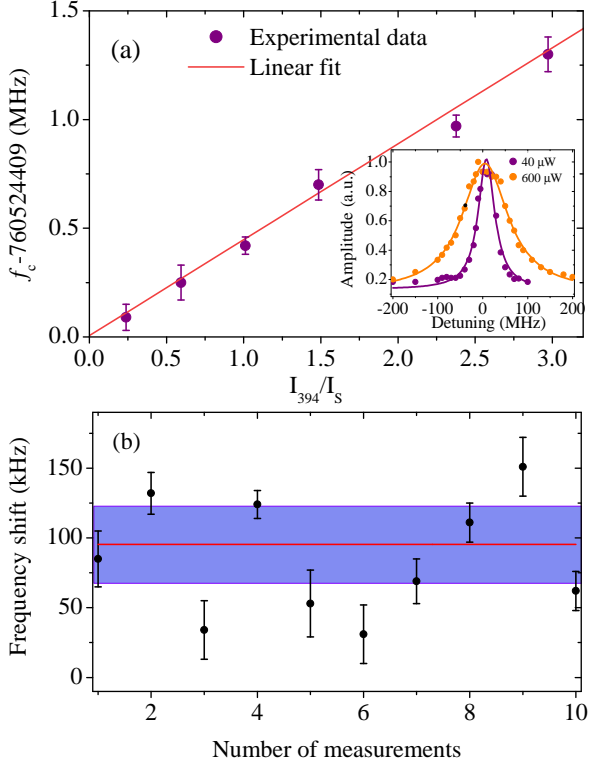


FIG. 8: (a) Dependence of line centre of  ${}^3P_0 \rightarrow {}^3D_1$  on the probe intensity for  ${}^{88}\text{Sr}$ . The filled circles and error bars are experimental data and  $1\sigma$  uncertainty, respectively. The red line is a fit to the data points. The inset shows the spectra under the probe power of  $40$  and  $600 \mu\text{W}$ . (b) Ten-times repeated measurements of  ${}^{88}\text{Sr}$  frequency. The red line is a weighted mean value of  $94 \text{ kHz}$  and the shaded area indicates the  $95\%$  confidence interval (CI) of  $55.1 \text{ kHz}$ .

## 3. Misalignment and line profile

Due to the imperfect wavefront overlapping [57], the misalignment of the retro-reflected probe beam was verified to be a key factor in our experiment for the frequency shifts and uncertainties. To assess this effect, we followed the proposed method in Ref [58] by deliberately misaligning the retro-reflected beam until the resonance intensity was reduced to  $50\%$ . A frequency shift in a range of  $0.2 \sim 1 \text{ MHz}$  was observed for each isotope. We conservatively estimated the frequency shift due to the misalignment to be  $20\%$  of the frequency shift under the half-intensity-drop misalignment, i.e.,  $40 \sim 200 \text{ kHz}$ . The resulting uncertainty was determined to be  $10\%$  of the frequency shift. In addition, the probe beam may cause the asymmetry in the recorded spectral line profile [59] due to the retro-reflected power loss by  $5 \sim 8\%$  due to the view port and the mirror. In fact, we didn't experimentally observe significant shifts by the line profile asymmetry under  $70 \mu\text{W}$  of the probe laser. Yet we conservatively assumed its uncertainty to be  $4 \text{ kHz}$  for each

isotope in order to include the effect of the asymmetry in the frequency analysis.

#### 4. Quadratic Zeeman shift

Since  $\pi$  transitions ( $\Delta m=0$ ) were driven by the linearly polarized probe beam, the linear Zeeman shift cancels out for all isotopes. However, the quadratic Zeeman shift [22, 60] arising from Zeeman coupling between  $^3D_1$  and  $^3D_2$  states is a considerable factor when the remaining magnetic field is non-negligible in our experiment. As the separation of  $^3P_J$  states is much larger than that of  $^3D_J$ , we only considered the quadratic Zeeman shift of  $^3D_1$ .

To estimate the quadratic Zeeman shift, we calculated Zeeman matrix elements  $\langle ^3D_1 | H_z | ^3D_2 \rangle$  in LS coupling for all isotopes. For even isotopes, the matrix element was calculated to be  $\langle ^3D_1, m=0 | H_z | ^3D_2, m=0 \rangle = 8.2$  MHz  $mT^{-1}B$ , yielding a quadratic Zeeman shift of 5.5 kHz at the magnetic field of  $\sim 3.5$  mT introduced by surrounding ion pumps and Zeeman slower magnets. Yet in terms of the odd isotope, i.e.,  $^{87}\text{Sr}$ , each Zeeman substate is coupled with multiple substates of  $^3D_2$ , which dramatically increases the computation complexity. In this work, we only focused on  $|F, m=11/2\rangle$ ,  $|F, m=9/2\rangle$  and  $|F, m=7/2\rangle$  substates of  $^3D_1$  to simplify the computing. The pure LS matrix elements are given by [61]

$$\langle J'Fm | H_z | JFm \rangle = \frac{(g_S - g_L)\mu_0 B}{4F(F+1)} \left\{ \frac{[(I+F+1)^2 - J^2][J^2 - (I-F)^2][J^2 - (l-1)^2][(l+2)^2 - J^2]}{J^2(4J^2-1)} \right\}^{\frac{1}{2}}, \quad (\text{D1})$$

$$\begin{aligned} \langle J'F-1m | H_z | JFm \rangle \\ = \frac{(g_S - g_L)\mu_0 B}{4JF} \left\{ \frac{(F^2 - m^2)[(J+F)^2 - (I+1)^2][(J+F)^2 - I^2][J^2 - (l-1)^2][(l+2)^2 - J^2]}{(4F^2-1)(4J^2-1)} \right\}^{\frac{1}{2}}. \end{aligned} \quad (\text{D2})$$

where  $J'$ ,  $J$  are  $^3D_1$  and  $^3D_2$ ;  $g_S=2$  and  $g_L=1$  are  $g$  factors associated with the spin and orbital angular momentum [48], respectively, and  $\mu_0$  is the Bohr magneton.

For  $^3D_1 |F, m=11/2\rangle$ , the matrix elements were calculated to be  $|\langle ^3D_1, F, m=11/2 | H_z | ^3D_2, F, m=11/2 \rangle|^2 = 34$  MHz $^2mT^{-2}B^2$  and  $|\langle ^3D_1, F, m=11/2 | H_z | ^3D_2, F=13/2, m=11/2 \rangle|^2 = 15$  MHz $^2mT^{-2}B^2$ . For the  $\Delta m=0$  transition, the quadratic Zeeman shift  $\Delta\nu_{Z2}$  is given by [48]

$$\Delta\nu_{Z2} = \sum_{F'} \frac{|\langle ^3D_1, F, m_F | H_z | ^3D_2, F', m_F \rangle|^2}{\nu_{^3D_2, F'} - \nu_{^3D_1}} \quad (\text{D3})$$

Thus, by summing up hyperfine states  $F'$  of  $^3D_2$  with the same  $m_F$ , the quadratic Zeeman shift can be calculated. The shift of  $|F, m=11/2\rangle$  was calculated by Eq. (D3) to be 4(0.04) kHz at the magnetic field of 3.5 mT. Similarly, other matrix elements were also calculated, which are  $|\langle ^3D_1, F, m=9/2 | H_z | ^3D_2, F, m=9/2 \rangle|^2 = 52$  MHz $^2mT^{-2}B^2$ ,  $|\langle ^3D_1, F, m=9/2 | H_z | ^3D_2, F=11/2, m=9/2 \rangle|^2 = 47$  MHz $^2mT^{-2}B^2$  and  $|\langle ^3D_1, F, m=7/2 | H_z | ^3D_2, F=9/2, m=7/2 \rangle|^2 = 5$  MHz $^2mT^{-2}B^2$ . The resulting quadratic Zeeman shifts for  $|F, m=9/2\rangle$  and  $|F, m=7/2\rangle$  are 5(0.05) kHz and 4(0.04) kHz, respectively, where the numbers in the bracket are the uncertainty due to the measurement of the magnetic field by 10% error. Therefore, by weighting the shifts of three Zeeman substates, the quadratic Zeeman shift of the centre of gravity for  $^{87}\text{Sr}$  was calculated to be 4.3(0.04) kHz.

#### 5. Other shifts

We calculated two other frequency shifts, i.e., photon recoil shift and the second-order Doppler shift. The photon recoil frequency shift was calculated to be 15 kHz by  $\delta\nu = h/(2m\lambda^2)$  [59], and the second-order Doppler shift was 2 mHz according to  $\delta\nu = v^2 f/(2c^2)$  [62] at the most probable speed of 0.7 m/s of the ensemble during the measurements. Some other shifts were not considered as they were negligible in our measurements.

---

[1] G. Breit, Rev. Mod. Phys. **30**, 507 (1958).  
[2] P. Campbell, I. Moore, and M. R. Pearson, Prog. Part. Nucl. Phys. **86**, 127 (2016).  
[3] G. Ewald, W. Nörtershäuser, A. Dax, S. Götte, R. Kirchner, H.-J. Kluge, T. Kühl, R. Sanchez, A. Wojtaszek, B. A. Bushaw, G. W. F. Drake, Z.-C. Yan, and C. Zimmermann, Phys. Rev. Lett. **93**, 11 (2004).  
[4] W. Nörtershäuser, R. Sánchez, G. Ewald, A. Dax, J. Behr, P. Bricault, B. A. Bushaw, J. Dilling, M. Dombrowsky, G. W. F. Drake, S. Götte, H.-J. Kluge, T. Kühl, J. Lassen, C. D. P. Levy, K. Pachucki, M. Pearson, M. Puchalski, A. Wojtaszek, Z.-C. Yan, and C. Zimmer-

TABLE III: Systematic frequency shifts and uncertainties (kHz) for the  ${}^3P_0 \rightarrow {}^3D_1$  transition for all Sr isotopes. Uncertainties indicate  $1\sigma$  deviation.

Contributors	88		84		86		87	
	Corr.	Unc.	Corr.	Unc.	Corr.	Unc.	Corr.	Unc.
Probe power shift	-94	13	-112	16	-101	14	-73	8
Density shift	183	16	203	17	197	16	142	11
Recoil shift	-15	<0.1	-15	<0.1	-15	<0.1	-15	<0.1
Misalignment	93	9.3	101	10.1	96	9.6	71	7.1
$2^{nd}$ order Doppler shift	2 mHz	<0.1 mHz						
Line profile	0	4	0	4	0	4	0	4
Quadratic Zeeman shift	5.5	<0.1	5.5	<0.1	5.5	<0.1	4.3	<0.1
Total	173	23	183	26	183	24	129	16

TABLE IV: Systematic frequency shifts and uncertainties (kHz) for ISs. Uncertainties indicate  $1\sigma$  deviation.

Contributors	88-84		88-86		88-87	
	Corr.	Unc.	Corr.	Unc.	Corr.	Unc.
Probe power shift	18	21	7	19	-21	15
Density shift	-20	23	-14	23	41	19
Recoil shift	0	<0.1	0	<0.1	0	<0.1
Misalignment	-8	14	-3	13	22	12
$2^{nd}$ order Doppler shift	0	$<10^{-7}$	0	$<10^{-7}$	0	$<10^{-7}$
Line profile	0	5.7	0	5.7	0	5.7
Quadratic Zeeman shift	0	<0.1	0	<0.1	1.2	<0.1
Total	-10	35	-10	33	43	28

mann, Phys. Rev. A **83**, 012516 (2011).

[5] I. Angeli and K. P. Marinova, At. Data Nucl. Data Tables **99**, 69 (2013).

[6] V. A. Dzuba, W. R. Johnson, and M. S. Safronova, Phys. Rev. A **72**, 022503 (2005).

[7] F. Gebert, Y. Wan, F. Wolf, C. N. Angstmann, J. C. Berengut, and P. O. Schmidt, Phys. Rev. Lett. **115**, 053003 (2015).

[8] M. R. Kalita, J. A. Behr, A. Gorelov, M. R. Pearson, A. C. DeHart, G. Gwinner, M. J. Kossin, L. A. Orozco, S. Aubin, E. Gomez, M. S. Safronova, V. A. Dzuba, and V. V. Flambaum, Phys. Rev. A **97**, 042507 (2018).

[9] F. W. Knollmann, A. N. Patel, and S. C. Doret, Phys. Rev. A **100**, 022514 (2013).

[10] M. S. Safronova, D. Budker, D. DeMille, D. F. J. Kimball, A. Derevianko, and C. W. Clark, Rev. Mod. Phys. **90**, 025008 (2018).

[11] V. A. Dzuba, V. V. Flambaum, and S. Schiller, Phys. Rev. A **98**, 022501 (2018).

[12] C. Frugueule, E. Fuchs, G. Perez, and M. Schlaffer, Phys. Rev. D **96**, 015011 (2017).

[13] W. H. King, J. Opt. Soc. Am. **53**, 638 (1963).

[14] W. H. King, *Isotope Shifts in Atomic Spectra* (Plenum, New York, 1984).

[15] V. V. Flambaum, A. J. Geddes, and A. V. Viatkina, Phys. Rev. A **97**, 032510 (2018).

[16] V. V. Flambaum and V. A. Dzuba, Phys. Rev. A **100**, 032511 (2019).

[17] S. O. Allehabi, V. A. Dzuba, V. V. Flambaum, and A. V. Afanasjev, Phys. Rev. A **103**, L030801 (2021).

[18] P. Munro-Laylim, V. A. Dzuba, and V. V. Flambaum, Phys. Rev. A **105**, 042814 (2022).

[19] K. Mikami, M. Tanaka, and Y. Yamamoto, Eur. Phys. J. C **77**, 896 (2017).

[20] J. C. Berengut, C. Delaunay, A. Geddes, and Y. Soreq, Phys. Rev. Res. **2**, 043444 (2020).

[21] J. C. Berengut, D. Budker, C. Delaunay, V. V. Flambaum, C. Frugueule, E. Fuchs, C. Grojean, R. Harnik, R. Ozeri, G. Perez, and Y. Soreq, Phys. Rev. Lett. **120**, 091801 (2018).

[22] F. W. Knollmann, A. N. Patel, and S. C. Doret, Phys. Rev. A **100**, 022514 (2019).

[23] C. Solaro, S. Meyer, K. Fisher, J. C. Berengut, E. Fuchs, and M. Drewsen, Phys. Rev. Lett. **125**, 123003 (2020).

[24] N. L. Figueiroa, J. C. Berengut, V. A. Dzuba, V. V. Flambaum, D. Budker, and D. Antypas, Phys. Rev. Lett. **128**, 073001 (2022).

[25] K. Ono, Y. Saito, T. Ishiyama, T. Higomoto, T. Takano, Y. Takasu, Y. Yamamoto, M. Tanaka, and Y. Takahashi, Phys. Rev. X **12**, 021033 (2022).

[26] I. Counts, J. Hur, D. P. L. A. Craik, H. Jeon, C. Leung, J. C. Berengut, A. Geddes, A. Kawasaki, W. Jhe, and V. Vuletić, Phys. Rev. Lett. **125**, 123002 (2020).

[27] J. Hur, D. P. L. A. Craik, I. Count, E. Knyazev, L. Caldwell, C. Leung, S. Pandey, J. C. Berengut, A. Geddes, W. Nazarewicz, P. G. Reinhard, A. Kawasaki, H. Jeon, W. Jhe, and V. Vuletić, Phys. Rev. Lett. **128**, 163201 (2022).

[28] M. Takamoto, F. Hong, R. Higashi, and H. Katori, Nat. **435**, 321 (2005).

[29] B. J. Bloom, T. L. Nicholson, J. R. Williams, S. L. Campbell, M. Bishof, X. Zhang, W. Zhang, S. L. Bromley, and J. Ye, Nat. **506**, 71 (2014).

[30] A. D. Ludlow, M. M. Boyd, J. Ye, E. Peik, and P. O. Schmidt, Rev. Mod. Phys. **87**, 637 (2015).

[31] M. A. Norcia, M. N. Winchester, J. R. K. Cline, and J. K. Thompson, *Sci. Adv.* **2**, e1601231 (2016).

[32] S. A. Schäffer, M. Tang, M. R. Henriksen, A. A. Jørgensen, B. T. R. Christensen, and J. W. Thomsen, *Phys. Rev. A* **101**, 013819 (2020).

[33] Y. Zhang, C. Shan, and K. Mølmer, *Phys. Rev. Lett.* **128**, 013604 (2022).

[34] S. Stellmer, M. K. Tey, B. Huang, R. Grimm, and F. Schreck, *Phys. Rev. Lett.* **103**, 200401 (2009).

[35] S. Stellmer, B. Pasquiou, R. Grimm, and F. Schreck, *Phys. Rev. Lett.* **110**, 263003 (2013).

[36] C.-C. Chen, R. G. Escudero, J. Minář, B. Pasquiou, S. Bennetts, and F. Schreck, *Nat.* **606**, 683 (2022).

[37] P. G. Mickelson, Y. N. M. de Escobar, P. Anzel, B. J. DeSalvo, S. B. Nagel, A. J. Traverso, M. Yan, and T. C. Killian, *J. Phys. B: At. Mol. Opt. Phys.* **42**, 235001 (2009).

[38] H. Miyake, N. C. Pisenti, P. K. Elgee, A. Sitaram, and G. K. Campbell, *Phys. Rev. Res.* **1**, 033113 (2019).

[39] S. Stellmer and F. Schreck, *Phys. Rev. A* **90**, 022512 (2014).

[40] F. Hu, I. Nosske, L. Couturier, C. Tan, C. Qiao, P. Chen, Y. H. Jiang, B. Zhu, and M. Weidemüller, *Phys. Rev. A* **99**, 033422 (2019).

[41] S. Zhang, P. Ramchurn, M. Menchetti, Q. Ubaid, J. Jones, K. Bongs, and Y. Singh, *J. Phys. B: At. Mol. Opt. Phys.* **53**, 235301 (2020).

[42] B. Olmos, D. Yu, Y. Singh, F. Schreck, K. Bongs, and I. Lesanovsky, *Phys. Rev. Lett.* **110**, 143602 (2013).

[43] X. Zhou, X. Xu, X. Chen, and J. Chen, *Phys. Rev. A* **81**, 012115 (2010).

[44] S. Subhankar, A. Restelli, Y. Wang, S. L. Rolston, and J. V. Porto, *Rev. Sci. Instrum.* **90**, 043115 (2019).

[45] N. Seymour-Smith, P. Blythe, M. Keller, and W. Lange, *Rev. Sci. Instrum.* **81**, 075109 (2010).

[46] E. C. SELTZER, *Phys. Rev.* **188**, 1916 (1969).

[47] R. E. Silverans, P. Lievens, L. Vermeeren, E. Arnold, W. Neu, R. Neugart, K. Wendt, F. Buchinger, E. B. Ramsay, and G. Ulm, *Phys. Rev. Lett.* **60**, 2607 (1988).

[48] M. M. Boyd, T. Zelevinsky, A. D. Ludlow, S. Blatt, T. Zanon-Willette, S. M. Foreman, and J. Ye, *Phys. Rev. A* **76**, 022510 (2007).

[49] C. S. Kischkel, M. Baumann, and E. Kümmel, *J. Phys. B: At. Mol. Opt. Phys.* **24**, 4845 (1991).

[50] Nist spectra database.

[51] J. Gütde, A. Klinkmüller, P. J. West, and E. Matthias, *Phys. Rev. A* **47**, 6 (1993).

[52] K. Beloy, A. Derevianko, and W. R. Johnson, *Phys. Rev. A* **77**, 012512 (2008).

[53] I. I. Sobel'man, *Introduction to the theory of atomic spectra* (Pergamon, Braunschweig, 1972).

[54] C. E. Moore and H. N. Russell, *J. Res. Natl. Bur. Stand.* **48**, 1 (1952).

[55] K. Hashiguchi, T. Akatsuka, N. Ohmae, M. Takamoto, and H. Katori, *Phys. Rev. A* **100**, 042513 (2019).

[56] T. Ido, T. H. Loftus, M. M. Boyd, A. D. Ludlow, K. W. Holman, and J. Ye, *Phys. Rev. Lett.* **94**, 153001 (2005).

[57] M. T. Herd, E. C. Cook, and W. D. Williams, *Phys. Rev. A* **104**, 042812 (2021).

[58] C.-M. Wu, T.-W. Liu, M.-H. Wu, R.-K. Lee, and W.-Y. Cheng, *Opt. Lett.* **38**, 16 (2013).

[59] X. Zheng, Y. R. Sun, J.-J. Chen, W. Jiang, K. Pachucki, and S.-M. Hu, *Phys. Rev. Lett.* **119**, 263002 (2017).

[60] K. J. Arnold, R. Kaewuam, S. R. Chanu, T. R. Tan, Z. Zhang, and M. D. Barrett, *Phys. Rev. Lett.* **124**, 193001 (2020).

[61] A. Lurio, M. Mandel, and R. Novick, *Phys. Rev.* **126**, 5 (1962).

[62] A. D. Brandt, S. F. Cooper, C. Rasor, Z. Burkley, A. Matveev, and D. C. Yost, *Phys. Rev. Lett.* **128**, 023001 (2022).